Angular momentum driven dynamics of stimulated Brillouin scattering in multimode fibers

Aaron P. Greenberg, Zelin Ma, and Siddharth Ramachandran*

Boston University, 8 Saint Mary's Street, Boston, MA, 02215, USA
sidr@bu.edu

Abstract: The strength of stimulated Brillouin scattering (SBS) in optical fibers is largely governed by the spatial overlap between supported optical and acoustic modes, leading to a complicated amalgamation of photon-phonon interactions in multimode fibers. Here, we study SBS dynamics in ring-core fibers that support modes carrying orbital angular momentum (OAM), which result in distinctive characteristics. We find that the OAM SBS response, as well as modal content, strongly depends on the polarization state of the pump, as OAM modes in fiber have distinct propagation dynamics depending on whether the input is circularly or linearly polarized. This is in contrast to conventionally posited wisdom that SBS strength is independent of the pump's input polarization state in an isotropic material. This increased specificity can lead to interesting effects such as spatial phase conjugation even in the presence of stably transmitted, i.e. non-aberrated, spatial pump modes. More generally, we show that using OAM modes yields additional degrees of control over SBS interactions beyond more conventional parameters, such as effective area, acousto-optic spatial overlaps, and material composition.

1. Introduction

Stimulated Brillouin scattering (SBS) is an important acousto-optic nonlinearity in optical fibers that has led to a variety of applications [1], including distributed sensing [2], light amplification [3], and slow light generation [4]. SBS is also a debilitating phenomenon that can act as a limitation for high powered fiber lasers [5,6] or impact long-haul communication systems [7,8]. As such, there is a desire to suppress SBS, or at least make it more controllable, which so far has been achieved mainly through waveguide design that changes the interactions between light and sound or by spectrally broadening the pump source [9,10]. SBS is also well known as one of the easiest and most reliable ways of producing phase conjugation [11], which is of interest for uses in aberration correction [12,13], optical trapping [14], and signal processing [15]. SBS has been extensively studied for conventional eigenmodes in multimode fibers [16–19]. But since modes in an optical fiber can also be expressed in terms of the orbital angular momentum (OAM) and spin angular momentum (SAM) they carry, SBS can also be analyzed in this modal basis. Here, we show that fibers stably guiding a large ensemble of high order OAM modes yield new forms of control over the SBS process due to modified mode selection rules and phase matching criteria, which also leads to the spontaneous generation of record high order OAM acoustic waves.

The OAM carried by optical fiber modes is quantified by a topological charge $\pm\mathcal{L}$ that represents the directional twisting of the helical phase front per wavelength [20]. The SAM carried by these fiber modes is represented by its left or right circular polarization state, $\hat{\sigma}^\pm$, respectively. Confined by a fiber in which they stably propagate [21], these supported $\pm\mathcal{L}; \hat{\sigma}^\pm$ modes experience a spin-orbit interaction (SOI), which makes the propagation constant of the mode dependent on the chirality, or sign, associated with both their OAM and SAM. This SOI dependence on chirality leads to the emergence of circular birefringence in an otherwise circularly symmetric, isotropic

fiber, which changes the propagation constant of the left and right handed circularly polarized SAM states. Hence, linearly polarized light of given OAM, when introduced into these fibers, experiences optical activity (OA) [22] – i.e., linear polarization rotation with propagation, which mimics a property that has been traditionally associated with anisotropic chiral materials. We have found that this attribute – of distinct propagation behavior arising from SOI-induced chirality – plays a significant role in changing the dynamics of SBS of these fiber modes. In the case of circularly polarized OAM-carrying pumps $\pm\mathcal{L}; \hat{\sigma}^{\pm}$, highly multimoded Stokes is observed, whose modal content is dictated by spatial overlap integrals (in analogy to the observed behavior from conventional fiber modes in standard fibers) and angular momentum conservation. In contrast, linearly polarized OAM pumps $\mathcal{L}; \hat{x}$ that experience OA exhibit dramatically different SBS modal behavior. Specifically, we see the rotational evolution of the polarization forces all Stokes light into a spatially phase conjugated state, suppressing other SBS interactions. We demonstrate how the SBS behaviors for each polarization state, circular and linear, differ from one another, in stark contrast to SBS behavior in conventional fibers, where it is agnostic to pump polarization state [23]. This suggests that the OAM content of light represents an attractive toolbox with which to control SBS nonlinear interactions in optical fibers.

2. OAM propagation dynamics in fibers

The ring-core optical fibers in which we conduct our studies are designed to support a large count of mode-mixing-free, stable OAM optical modes ($|\mathcal{L}|>20$ at 1 μm wavelengths), hence yielding a highly multimoded platform in which to study SBS [24]. The fiber is an isotropic and circularly symmetric medium, which is shown by the image of the fiber facet in Fig. 1(a). To differentiate fiber modes, we consider the chirality, or sign, of $\mathcal{L}$ and $\hat{\sigma}$. If these two quantities match in sign, then the fiber mode is a spin-orbit aligned (SOa) mode, and if they are opposite, it is a spin-orbit anti-aligned (SOaa) mode. Their electric fields are given by:

$$E_{\pm\mathcal{L};\sigma^{\pm}} = A(z,t)F_{\mathcal{L}}(r) \left\{ \begin{array}{c} \hat{\sigma}^{\pm}\exp(\pm i|\mathcal{L}|\phi)\exp[i(\beta_{SOa}z)] \\ \hat{\sigma}^{\pm}\exp(\mp i|\mathcal{L}|\phi)\exp[i(\beta_{SOaa}z)] \end{array} \right\} \quad (1)$$

where $A(z,t)$ is the complex amplitude envelope, $F_{\mathcal{L}}(r)$ is the mode field profile, z is the fiber propagation length, and SOa / SOaa propagation constants are $\beta_{SOa} = 2\pi \cdot n_{eff}^{SOa}/\lambda$ and $\beta_{SOaa} = 2\pi \cdot n_{eff}^{SOaa}/\lambda$, proportional to their effective indices n_{eff}^{SOa} and n_{eff}^{SOaa}, respectively. These distinct n_{eff} for $\hat{\sigma}^{\pm}$ OAM modes stem from the SOI, as it is responsible for splitting the effective indices between SOa and SOaa modes with the same $\mathcal{L}$ topological charge, such that $\Delta n_{eff}(\mathcal{L},\lambda) = n_{eff}^{SOa}(\mathcal{L},\lambda) - n_{eff}^{SOaa}(\mathcal{L},\lambda)$, effectively making the fiber a circularly birefringent medium. The ring-core fiber's refractive index profile, Δn (relative to silica) is shown in Fig. 1(b), which illustrates our fiber's large index gradients, $\partial\Delta n(r)/\partial r$, at core boundaries. This design enhances the SOI in accordance with $\Delta n_{eff} \propto \mathcal{L} \int F_{\mathcal{L}}^2(r)\frac{\partial\Delta n(r)}{\partial r}dr$ [21], which has been found to simplify to $\Delta n_{eff} \propto \mathcal{L}^3$ [25]. Figure 1(c) shows experimentally recorded near-field images of select OAM modes in this fiber. Also shown in the right of each of these images are near-field images of the modes after they pass through a titled lens (number of dark fringes $= |\mathcal{L}|$, and their orientation specified by the sign of $\mathcal{L}$ [26]). These fiber modes are known to propagate stably in ring-core fibers such that their amplitudes and polarization states are maintained and are robust to perturbations, such as bends [27]. This is schematically illustrated in Fig. 1(d), with a mode's intensity profile (grey rings) and circular polarization (red circles) preserved throughout the fiber. Following from Eq. (1), the electric field of a superposition of oppositely polarized OAM modes with the same $\mathcal{L}$, equivalent to a linearly polarized state $(\hat{\sigma}^+ + \hat{\sigma}^-) = \hat{x}$, may be represented as:

$$E_{\mathcal{L};x} = A(z,t)F_{\mathcal{L}}(r)\exp(\pm i|\mathcal{L}|\phi)\exp[i(\beta_{avg}z)][\hat{x}\cos(\gamma) \mp \hat{y}\sin(\gamma)] \quad (2)$$

where $\beta_{avg} = (\beta_{SOa} + \beta_{SOaa})/2$ and $\gamma = z\pi\Delta n_{eff}/\lambda$ is the linear polarization angle at position z in the fiber. It is apparent from Eq. (2) that the OA state's linear polarization state rotates as it propagates – as depicted in Fig. 1(e). The rotation rate is proportional to γ, which, as the above equations show, is proportional to $\mathcal{L}^3$, meaning the rotational rate experienced by the OAM modes is highly contingent on its topological charge. One would normally posit that this linear polarization state is rather unstable in the fiber because it arises from a modal phase difference, which are usually not stable in multimode fibers. However, one peculiarity of this SOI-induced birefringence is that, being geometrodynamic in nature, it is considerably stable [22]. This allows for the systematic study of SBS dynamics of OAM modes in ring-core fibers.
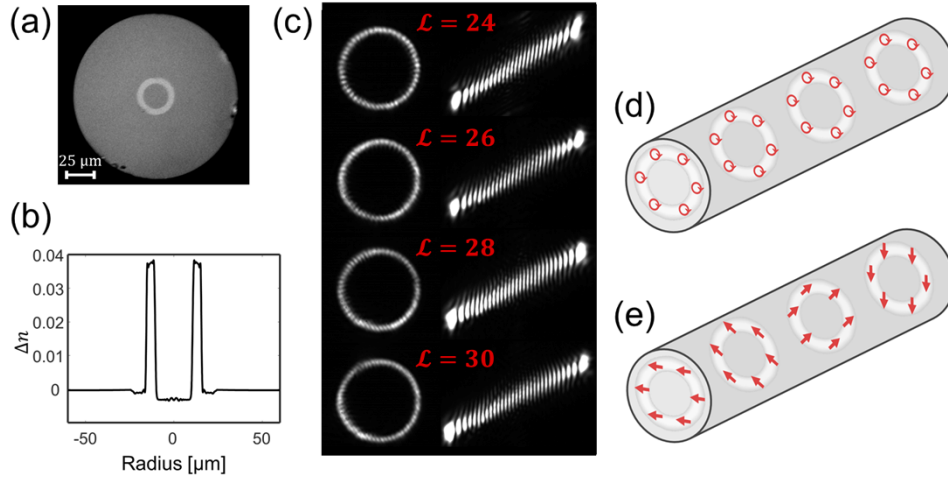

Fig. 1. (a) A fiber facet image of the circularly symmetric and isotropic ring-core fiber. (b) The 1D index profile of the ring-core fiber, plotted as Δn with respect to silica. The large index gradients of the core enhance the SOI that leads to circular birefringence in the fiber. (c) Intensity profiles of OAM modes out of the ring-core fiber are presented on the left. Each mode's topological charge is determined with a tilted lens and is equal to the number of dark fringes; these images (which are horizontally scaled) are presented on the right. (d) The evolution of an OAM mode with circular polarization (red circles) propagating through the fiber. Both the mode's amplitude (grey rings) and polarization are preserved throughout the fiber. (e) The evolution of an OAM superposition state with linear polarization (red arrows) propagating through the fiber. These states preserve their amplitudes (grey rings), but experience optical activity, or rotation of linear polarization with propagation, which is illustrated by the changing arrow orientations.

3. OAM SBS responses and setup

SBS gain g, in optical fibers can be characterized by an acousto-optic effective area A_{eff}^{ao} [1]. In spatial modes that carry OAM and SAM, angular momentum must also be conserved, a principle that has been demonstrated in previous works [28–30]. Heterodyne measurements along with waveguide eigenvalue calculations (measurements, matching calculations within 1.23%, are described later in section 4.2) affirm that the SBS we observe is a result of dominating axial-strain / longitudinal displacement acoustic modes u_z, which are described with complex envelope $\tilde{\rho}(z, t)$, acoustic frequency Ω, and propagation constant q [1].

$$u_z = \tilde{\rho}(z,t)\rho_{\mathcal{L}}(r)\exp(\pm i|\mathcal{L}|\phi)\exp[i(qz - \Omega t))] \tag{3}$$

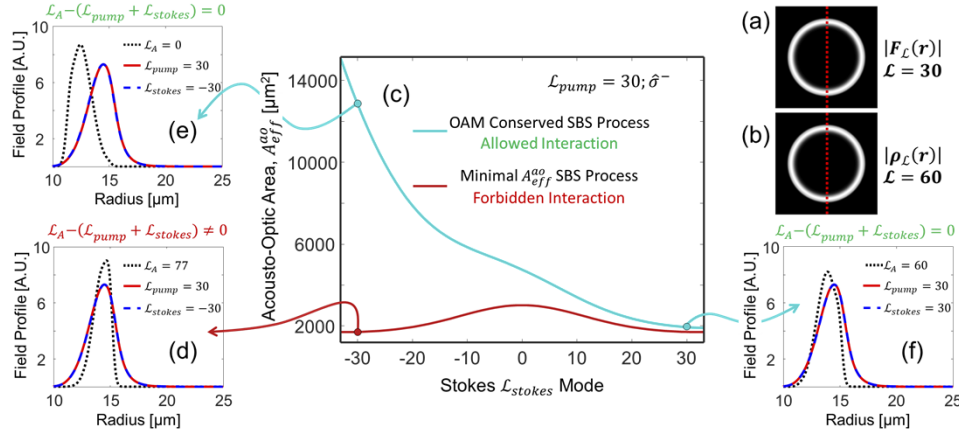**Fig. 2. Spatial field overlaps and acousto-optic areas:** calculated using a $\mathcal{L}_{pump} = 30$; $\hat{\sigma}^-$ pump. (a) 2D profile of $|F_{\mathcal{L}}(r)|$ for an optical OAM mode with topological charge $\mathcal{L} = 30$, with a 1D radial linecut marked in red. (b) 2D profile of $|\rho_{\mathcal{L}}(r)|$ for an acoustic mode with topological charge $\mathcal{L} = 60$, with a 1D radial linecut marked in red. (c) The blue curve plots A_{eff}^{ao} for the allowed SBS interactions that follow the OAM conservation condition $\mathcal{L}_A = \mathcal{L}_{pump} + \mathcal{L}_{stokes}$ that are supported by our ring-core fiber. On the other hand, the red curve plots the minimal A_{eff}^{ao} (i.e. – maximum spatial overlap) possible for each combination of pump, Stokes, and acoustic mode, even if it is a forbidden interaction that ignores OAM conservation. (d) Ignoring the OAM conservation condition, the process where the pump reflects into a Stokes mode, $\mathcal{L}_{stokes} = -\mathcal{L}_{pump}$ could have high radial spatial overlap with an acoustic $\mathcal{L}_A = 77$ mode, with an $A_{eff}^{ao} = 1701\mu m^2$. (e) However, in order to be an allowed process that satisfies OAM conservation, these optical modes must instead interact with a lower order and spatially separated $\mathcal{L}_A = 0$ phonon, resulting in low radial spatial overlap and hence a large $A_{eff}^{ao} = 12868\mu m^2$. (f) Likewise, the phase conjugated SBS interaction of $\mathcal{L}_{stokes} = \mathcal{L}_{pump}$ requires, due to OAM conservation, interaction with a high order $\mathcal{L}_A = 60$ phonon, resulting in high radial spatial overlap with $A_{eff}^{ao} = 1931 \mu m^2$. Hence, OAM conservation changes SBS dynamics to favor interactions closer to the phase conjugated process ($\mathcal{L}_{stokes} = \mathcal{L}_{pump}$), in which modes possess high spatial overlap, and disfavors interactions closer to the reflected SBS process ($\mathcal{L}_{stokes} = -\mathcal{L}_{pump}$), in which modes are spatially separated.

As we can see from Eq. (3), these acoustic phonons can carry the OAM helical phase with charge $\mathcal{L}$, but since they are longitudinally polarized, they cannot carry SAM. This means that SAM conservation is satisfied only between the pump and Stokes optical fields, while OAM conservation is achieved through the interplay of all participating optical and acoustic modes. For a pump with OAM $\mathcal{L}_{pump}$ and Stokes in a spatial mode with OAM $\mathcal{L}_{stokes}$, the well-known expression for acousto-optic effective area can be written in a modified form of [1,31]:

$$g \propto {}^1\!/_{A_{eff}^{ao}} \propto \frac{\left[\iint F_{\mathcal{L}_{pump}}^* \cdot \rho_{\mathcal{L}_A} \cdot F_{\mathcal{L}_{stokes}} e^{i[\mathcal{L}_A - (\mathcal{L}_{pump} + \mathcal{L}_{stokes})]\phi} dA \right]^2}{\iint |F_{\mathcal{L}_{pump}}|^2 dA \cdot \iint |\rho_{\mathcal{L}_A}|^2 dA \cdot \iint |F_{\mathcal{L}_{stokes}}|^2 dA} \qquad (4)$$

where $\rho_{\mathcal{L}_A}(r)$ is the displacement profile of longitudinal acoustic modes carrying topological charge $\mathcal{L} = \mathcal{L}_A$ (see Eq. (3)). We see that the OAM conservation condition acts to impose a mode selection rule on SBS, such that the only allowed acousto-optic interactions are those that meet the condition $\mathcal{L}_A - (\mathcal{L}_{pump} + \mathcal{L}_{stokes}) = 0$. Since a fiber that guides multiple optical modes also typically guides several (in fact, many more) acoustic modes, finding an acoustic mode with

appropriate $\mathcal{L}_A$ to allow for OAM conservation is easy. In Fig. 2 we show A_{eff}^{ao} calculations, for the fiber depicted in Fig. 1, for a SOaa $\mathcal{L}_{pump} = 30; \hat{\sigma}^-$ pump, to illustrate the role that OAM conservation plays in dictating SBS interaction strengths and modal content. The 2D field profiles $F_{\mathcal{L}}(r)$ and $\rho_{\mathcal{L}}(r)$ used in these calculations are simulated with optical and acoustic mode solvers, and are highlighted in Fig. 2(a) and 2(b), respectively (see Eq. (1) and Eq. (3)). We note that if OAM conservation is satisfied between these modes then we can trivially factor out the azimuthal spatial integral as 2π, allowing us to simplify our A_{eff}^{ao} calculations to a 1D radial spatial integral of $F_{\mathcal{L}}(r)$ and $\rho_{\mathcal{L}}(r)$ overlaps (radial profiles are taken from a linecut of the 2D profile). We first calculate spatial overlaps ignoring the OAM conservation condition and treat our fiber modes conventionally, where any combination of pump, Stokes, and acoustic mode can interact with one another. The resultant red curve in Fig. 2(c) suggests that the Stokes' gain is equally efficient in almost all available modes. For instance, the $\mathcal{L}_{pump} = 30$, $\mathcal{L}_{stokes} = -30$, and $\mathcal{L}_A = 77$ modes have significant spatial overlap (see Fig. 2(d)) and is reminiscent of conventional SBS scattering into the same optical mode in which the pump resides – i.e. $\mathcal{L}_{stokes} = -\mathcal{L}_{pump}$. We note that for this SBS process, the opposite sign on $\mathcal{L}$ arises from the fact that the two waves travel in opposite directions, making this emblematic of a 'reflected' process, as if it were bouncing off from a mirror. This would normally be a preferred process for SBS, but since OAM conservation is not satisfied, it is forbidden. The blue curve of Fig. 2(c) is the calculated A_{eff}^{ao} accounting for OAM conservation – i.e., a trace of the full Eq. (4). It is now evident that the reflected process has dramatically higher A_{eff}^{ao} since it requires interaction with the $\mathcal{L}_A = 0$ acoustic mode, which has poor spatial overlap with the optical modes (Fig. 2(e)). On the other hand, there is considerably high overlap of the high order acoustic mode (e.g. $\mathcal{L}_A = 60$ – see Fig. 2(f)) with the optical fields when $\mathcal{L}_{stokes} = \mathcal{L}_{pump}$, yielding a natural preference for Stokes modes closer to the OAM *conjugate* of the pump (i.e., a conjugate process that inverts OAM with a mode transformation of $\mathcal{L}_A = 2 \cdot \mathcal{L}_{pump}$, but again, because of the counter-propagating nature of these waves, becomes $\mathcal{L}_{stokes} = \mathcal{L}_{pump}$ in accordance with our sign convention used for the reflected process). The large difference between the blue and red curves shows how OAM conservation changes the inherent SBS dynamics of OAM carrying fiber modes to favor interactions closer to the phase conjugated process, while disfavoring interactions closer to the reflected process [31].

Another interesting observation is that the blue and red curves in Fig. 2(c) never cross. This indicates that the allowed SBS processes never produce an optimally overlapped acousto-optic interaction and there is always some spatial walk-off present between the optical and acoustic modes. This points to the proclivity of OAM conservation to reduce the SBS Stokes' gain. Focusing now on the phase conjugated $\mathcal{L}_{stokes} = \mathcal{L}_{pump} = 30$ interaction, we find that there are 14 other SBS interactions ($\mathcal{L}_{stokes} = 19$ to 33) with comparable $A_{eff}^{ao} \sim \pm 1$ dB, showing that many of these processes have similar strengths despite spanning a wide modal range. The fact that many of these SBS interactions have such similar acousto-optic effective areas is attributed to the near identical ring field profiles shared by OAM modes, which we presented in Fig. 1(c) (these strong spatial similarities of OAM modes are especially evident when compared to other modes supported in multimode fibers [32]). As such, we expect that, for a circularly polarized OAM pump, the generated Stokes light will be partitioned into a multitude of higher order modes. And, as we will see later, linearly polarized pumps experiencing chiral OA have an additional constraint that restricts the modes in which the Stokes occurs.

Our setup to test SBS with OAM modes is illustrated in Fig. 3(a). It uses a pump laser at 1045 nm that produces rectangular 1-μs pulses at a 5 kHz rep-rate with peak power exceeding 100 W (see Fig. 3(b)). To launch the forward-propagating OAM pump modes of interest into our 50-m ring-core fiber, the beam from our laser source is spatially sculpted with a spatial light modulator (SLM1) to impart it with topological charge $\mathcal{L}_{pump}$, while a rotating quarter wave plate (QWP) is used to set the polarization state as either circular $\hat{\sigma}^-$ or linear $\hat{x}$. We ensure that this combination of pulse length and fiber length would allow us to treat the SBS response as if

the pump were effectively a continuous-wave source, while avoiding any transient effects [33]. Additionally, for each $\mathcal{L}_{pump}$ mode that is used in our experiments pump power, $P_{pump}(\mathcal{L})$, is adjusted to compensate for the respective change in modal launch loss into the fiber, ensuring that all SBS responses are tested with effectively the same pump power. The injected pump peak powers into the fiber are $P_{pump}(24) = 29.3$ W, $P_{pump}(26) = 32.2$ W, $P_{pump}(28) = 32$ W, and $P_{pump}(30) = 35$ W. This is done by using a half wave plate (HWP1) and polarization beam splitter (PBS) to change the amount of $\hat{x}$ light incident on the polarization selective SLM. With these pump powers, we conduct our measurements above threshold power [1], i.e. in the high gain (strong scattering) regime [34]. The output of the fiber is imaged onto a CCD camera to perform mode purity analysis with spatial interferometry techniques [35], which verify >20 dB mode excitation purities, with polarization extinction ratios measured to be >15 dB. This means the pump is monomoded despite the fiber being multimoded. The back-scattered Stokes is redirected with a beam splitter (BS) to a mode sorter comprising another SLM2 (which applies an additional topological charge of $\mathcal{L}_{mode-sorter}$) and single mode fiber (SMF), which when sent to an optical spectrum analyzer (OSA), allows measuring modal power of the Stokes with extinction ratios >20 dB [24]. This mode sorting technique is also capable of separating Rayleigh back-reflected light from the SBS Stokes. Since Rayleigh scattered light exists exclusively in the $-\mathcal{L}_{pump}$ mode,
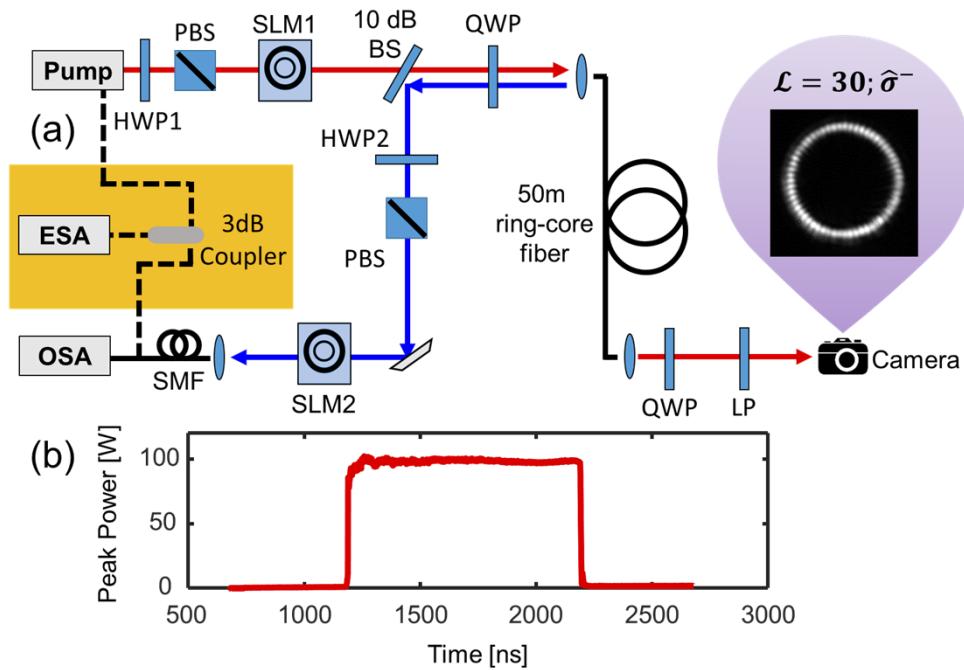

Fig. 3. (a) Experimental setup used to measure OAM SBS modal power and spectral characteristics from 50 m of ring-core fiber. The forward-propagating pump path is in red, while the back-propagating Stokes path is in blue. Following mode sorting, modal SBS gain is characterized through power measurements of the Stokes on an optical spectrum analyzer (OSA). This power setup can be modified to measure modal spectral characteristics by substituting in the spectrum analyzer (ESA), in the orange box, using a heterodyne configuration. Spectral interferometry on the pump output ($\mathcal{L} = 30$; $\hat{\sigma}^-$ OAM pump illustrated here) is used to measure, and maximize, mode purity. SLM – spatial light modulator, PBS – polarization beam splitter, BS – beam splitter, QWP – quarter wave plate, HWP – half wave plate, LP – linear polarizer, SMF – single mode fiber. (b) Example of a time-domain measured rectangular 1000 ns, 5kHz pulse from the pump source.

any applied $\mathcal{L}_{mode-sorter}$ that does not specifically select for it will transform the Rayleigh light into a $\mathcal{L}_{pump} + \mathcal{L}_{mode-sorter}$ OAM mode that does not couple into the SMF, effectively filtering it out. The power and absolute spectrum (10 pm resolution) of each sorted $\mathcal{L}_{stokes}$ mode is then measured with the OSA, and its RF spectrum is obtained by performing heterodyne measurements (orange shaded box in Fig. 3(a)) [36]. The heterodyne beat frequency between the pump and Stokes is measured with an electronic spectrum analyzer (ESA), which enables relative spectral measurements of the acoustic frequency and linewidth from each $\mathcal{L}_{stokes}$ spectrum with 10 kHz resolution. For the OA $\mathcal{L}; \hat{x}$ pump case, Stokes measurements are determined by combining OSA and ESA measurements taken at two orthogonal polarizations for each $\mathcal{L}_{stokes}$ sorted mode.

4. OAM SBS results

4.1. Stokes power measurements

First, we examine SBS dynamics utilizing circularly polarized SOaa $\mathcal{L}_{pump}; \hat{\sigma}^-$ modes as our pump. As an example, we use a pump mode with $\mathcal{L}_{pump} = 28$, while the mode sorter is set to $\mathcal{L}_{mode-sorter} = -28$. If the Stokes beam were comprised of only a single specific mode, the mode sorter would convert the back-scattered beam into a distinctive Bessel-beam pattern (in the far-field). Instead, as shown in Fig. 4(a), a massively multimoded beam is recorded (at first glance, it may appear Gaussian in shape, but we experimentally confirm it to resemble a speckle pattern comprising many modes). Quantifying this with OSA measurements (Fig. 4(b)) shows that the Stokes power in the representative modes $\mathcal{L}_{stokes} = [22, 28, 33]$ are similar, confirming the multimoded nature of the Stokes light, as deduced from the image of Fig. 4(a). We repeat these measurements with different pump modes, and summarize our findings in Fig. 4(c). The Stokes manifests over a broad range of backward propagating modes regardless of the topological charge of the pump. The mode with the highest Stokes power (yellow stars in Fig. 4(c)) shifts to increasingly higher order OAM modes, with exception of the $\mathcal{L}_{pump} = 30$ mode, where it appears to occur for a lower order mode. This drop in power for the $\mathcal{L} \geq 30$ modes is not a result of lower spatial overlaps from Eq. (4), but is instead due to the fact that the $\mathcal{L} \geq 30$ modes in our fiber are approaching cutoff and possess larger linear propagation losses [37]. We also observed negligible amounts of Stokes power in modes with $\mathcal{L}_{stokes}$ of opposite sign as $\mathcal{L}_{pump}$ – i.e. the reflected modes that would have interacted only with acoustic modes of low topological charges $\mathcal{L}_A$. We again note that Rayleigh reflected light in the $-\mathcal{L}_{pump}$ mode has been filtered out from the SBS Stokes power measurements as a result of us using our mode sorter to select for only $+|\mathcal{L}|$ modes. Hence, to summarize, SBS arising from pump modes that carry a well-defined OAM in a circular polarization state scatters light into a multitude of OAM Stokes modes that are generally close to $\mathcal{L}_{pump}$ while strongly preferring interactions involving very high acoustic OAM.

For the second round of measurements, we turn our attention to linearly polarized OA $\hat{x}$ states as our pump. Portrayed in Fig. 4(d) is the far-field Stokes image formed from a $\mathcal{L}_{pump} = 28$ and with the mode sorter set to $\mathcal{L}_{mode-sorter} = -28$, as before. In sharp contrast to Fig. 4(a), the image now depicts a clear Bessel-beam-like pattern, suggesting that the Stokes has been substantially generated in the $\mathcal{L}_{stokes} = 28$ mode alone. Quantitative power measurements with the OSA conducted at one HWP position (Fig. 4(e)) show that the Stokes power in modes with $\mathcal{L}_{stokes}$ adjacent to the phase conjugated state are nearly extinguished (note that this Fig. shows mode extinction of ~20 dB, which corresponds to the noise-floor of this measurement technique). The power matrix in Fig. 4(f) demonstrates a universal principle for linearly polarized pumps. The entirety of the produced Stokes power appears to exist only in the same $\mathcal{L}$ mode order as the pump, while the power in all other measured modes reside at the mode sorter noise floor. Note, as mentioned above, that we quantitatively measured Stokes power in only the adjacent mode orders – for mode orders further than $\mathcal{L}_{pump} \pm 2$, a full quantitative analysis was unnecessary since we qualitatively confirmed that negligible power existed in them.

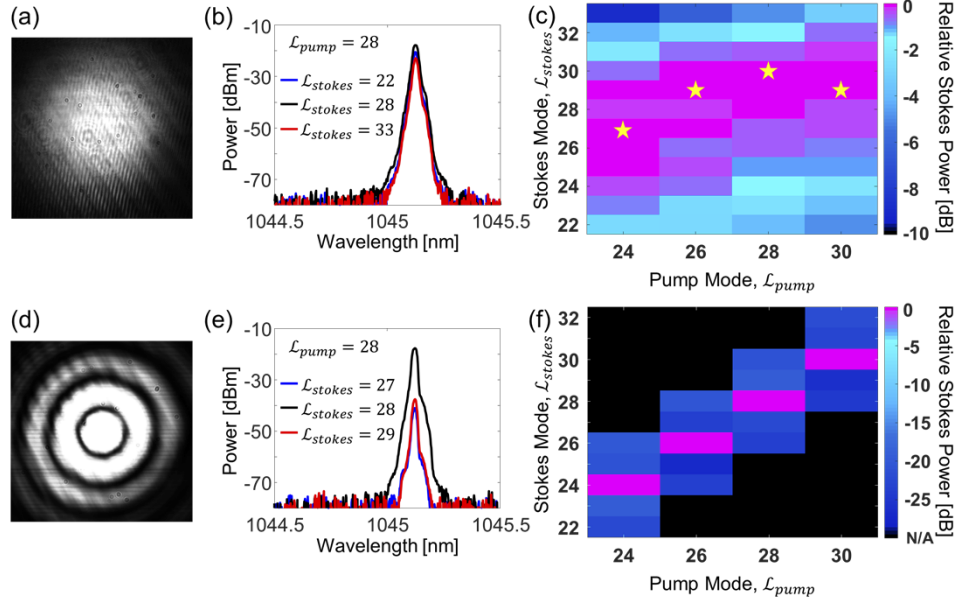**Fig. 4.** (a) Far-field image of SBS Stokes light generated from a $\mathcal{L}_{pump} = 28$; $\hat{\sigma}^-$ pump after a mode sorter configuration of $\mathcal{L}_{mode-sorter} = -28$. Despite its Gaussian appearance, the lack of a distinctive Bessel-beam-like pattern indicates there is interference between multiple modes. (b) OSA traces used to determine the modal power for each SBS interaction. Here we present measurements from $\mathcal{L}_{pump} = 28$; $\hat{\sigma}^-$, and power in $\mathcal{L}_{stokes} = [22, 28, 33]$. (c) Matrix of relative measured Stokes powers for each pump $\mathcal{L}_{pump} = [24, 26, 28, 30]$; $\hat{\sigma}^-$, demonstrating how the SBS gain partitions over the modal space of the fiber. The mode with the highest Stokes power for each pump is marked with a yellow star. (d) Far-field image of SBS Stokes light generated from a $\mathcal{L}_{pump} = 28$; $\hat{x}$ pump after a mode sorter configuration of $\mathcal{L}_{mode-sorter} = -28$. Here we see the back-scattered Stokes has been converted into a pure $\mathcal{L} = 0$ Bessel beam, indicating that all power resides in only the phase conjugated OA state, relative to the pump. (e) OSA traces at one (out of two) HWP positions needed to determine the modal power for each SBS interaction. Here we present measurements from $\mathcal{L}_{pump} = 28$; $\hat{x}$, and power in $\mathcal{L}_{stokes} = [27, 28, 29]$. (f) Matrix of relative measured Stokes powers for each pump $\mathcal{L}_{pump} = [24, 26, 28, 30]$; $\hat{x}$, demonstrating how all power channels into the phase conjugated state because of the strong effect that mode chirality has on SBS dynamics.

4.2. Heterodyne measurements

To further study the OAM SBS behavior of the acoustic vortices supported in our fiber, we conducted heterodyne measurements with the setup shown in Fig. 3(a). Figure 5(a) shows an ESA trace of the Stokes spectrum (blue), with an applied functional fit (red), generated from a $\mathcal{L}_A = 52$ acoustic phonon with circularly polarized $\mathcal{L}_{pump} = 26$ and $\mathcal{L}_{stokes} = 26$ modes. Since we are operating above threshold power, gain-narrowing effects validates the use of a Gaussian fit [34]. From this curve fitting we measure the Brillouin frequency and spectral linewidth of each $\mathcal{L}_A$ phonon. Figure 5(b) shows the acoustic frequencies for the different phonons, produced from various acousto-optic interactions over the modal space (sorted by which $\mathcal{L}_{pump}$ was used). Although all acoustic frequencies are measured to be around ~14 GHz, they are unique for each combination of participating [$\mathcal{L}_{pump}$; $\mathcal{L}_{stokes}$] optical fields. For example, the $\mathcal{L}_A = 54$ acoustic phonons associated with the [$\mathcal{L}_{pump} = 24$; $\mathcal{L}_{stokes} = 30$] and [$\mathcal{L}_{pump} = 30$;
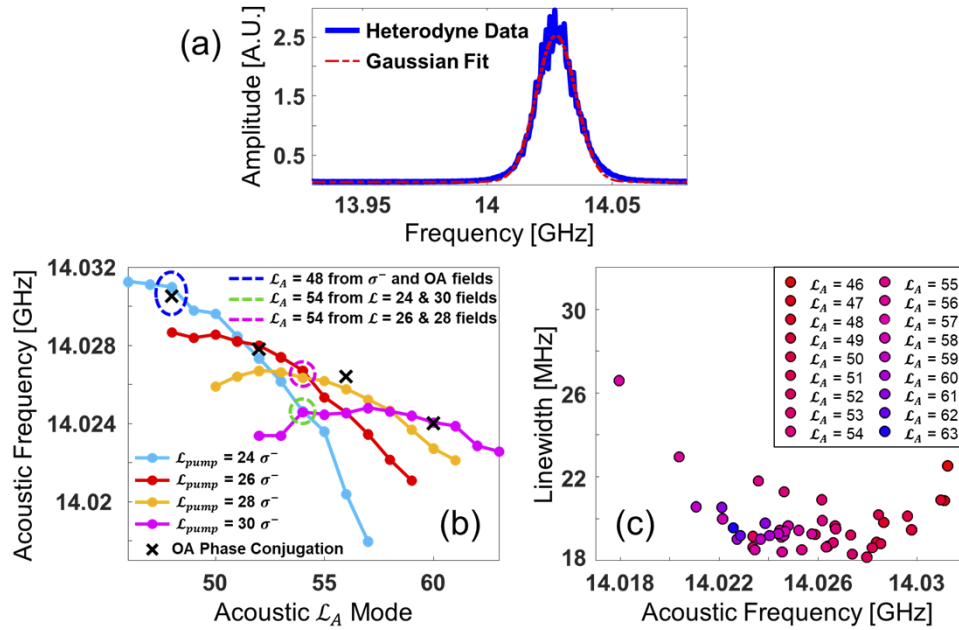
Fig. 5. (a) Heterodyne measurement raw data trace taken from the ESA, in blue, and an applied Gaussian fit, in red, for the circularly polarized pump mode $\mathcal{L}_{pump} = 26$ and Stokes mode $\mathcal{L}_{stokes} = 26$ (mediated by an acoustic phonon $\mathcal{L}_A = 52$). (b) Acoustic frequency measurements of each phonon $\mathcal{L}_A$ produced by SOaa $\mathcal{L}_{pump}$; $\hat{\sigma}^-$ pumps. These measurements reveal distinct and resolvable properties of the acoustic phonons depending on the OAM carried by the pump and Stokes. Phonons generated by the same OAM optical fields, regardless of which mode is the $\mathcal{L}_{pump}$ or $\mathcal{L}_{stokes}$, possess the same frequency, as highlighted by the $\mathcal{L}_A = 54$ generated phonons (see the green- and pink-dashed circles). The acoustic frequency is also independent of polarization (see an example in the blue-dashed oval), following conventional SBS phase matching principles. (c) Measured linewidths as a function of their respective frequencies (corresponding to their combination of $\mathcal{L}_{pump}$ and $\mathcal{L}_{stokes}$). We note that since we are operating above SBS threshold these acoustic phonons experience gain-narrowing effects, which is why nearly all linewidths are measured to be ~20 MHz.

$\mathcal{L}_{stokes} = 24$] interactions have the same frequency (green-dashed circle), but this is different from the $\mathcal{L}_A = 54$ phonons associated with the [$\mathcal{L}_{pump} = 26$; $\mathcal{L}_{stokes} = 28$] and [$\mathcal{L}_{pump} = 28$; $\mathcal{L}_{stokes} = 26$] interactions (which themselves have nearly the same measured frequencies, pink-dashed circle). We also performed these measurements using optically active linearly polarized pumps, specifically probing the OA phase conjugated acousto-optic interactions (black x's in Fig. 5(b)). Here we find that acoustic frequency is independent of the state of polarization used, as we see in the blue-dashed oval, where circularly and linearly polarized [$\mathcal{L}_{pump} = 24$; $\mathcal{L}_{stokes} = 24$] interactions produce acoustic phonons with very similar frequencies. This indicates that acoustic frequency is governed by the traditional SBS phase matching conditions between optical and acoustic modes [1]. Next, Fig. 5(c) shows the linewidth measurements of each phonon associated with the combinations of circularly polarized $\mathcal{L}_{pump}$ and $\mathcal{L}_{stokes}$ modes, as distinguished by the measured frequencies from Fig. 5(b). All linewidths are found to all be approximately 20 MHz (with the exception of certain Stokes modes generated from $\mathcal{L}_{pump} = 24$), which suggests that our phonons are indeed experiencing gain-narrowing [34]. Therefore, although the previous section showed distinctive mode-selection and polarization dependencies for OAM carrying pumps, the

associated acoustic frequencies and linewidths follow the well-established phase matching rules and dynamics for SBS in standard multimode fibers.

5. Discussion

The SBS measurements described in section 4 can be summarized as follows. When the pump is in a circular polarization state, carrying a well-defined topological charge $\mathcal{L}_{pump}$, backward propagating Stokes light scatters into a multitude of modes with topological charge close to the value of $\mathcal{L}_{pump}$. The highest power Stokes mode also appeared to prefer shifting towards higher mode orders, though this trend was seen to break down for $\mathcal{L}_{pump} = 30$, but, as we noted previously, that is simply because modes of $\mathcal{L} \geq 30$ become quite lossy in our fiber [37]. The reason for this is that the SBS process strongly prefers modes with $\mathcal{L}_{stokes}$ that is of the same sign and near the absolute value as that of $\mathcal{L}_{pump}$ – i.e. modes that have undergone a mode transformation mediated by very high order acoustic modes with $\mathcal{L}_A \approx 2 \cdot \mathcal{L}_{pump}$ – in accordance with the OAM conservation mode selection rule. It is interesting to note that the system naturally prefers to generate high OAM acoustic modes (as high as 63 in our experiments) in contrast to conventional SBS in standard fibers, which typically do not generate, or at least prefer, high OAM sound vibrations. But given Eq. (4), Fig. 2, and the discussion in section 3, this is not unexpected. The SBS process always chooses the mode combinations that result in high overlap integrals, and for high OAM charge pumps, these overlaps turn out to simply be with acoustic modes with roughly double the twist rates.

The SBS behavior observed with linearly polarized pumps carrying OAM is markedly different. These (pump) modes obviously have the same field amplitude profiles as circularly polarized modes, which may appear to imply that Eq. (4) and all the discussion from section 3 should predict similar behavior of that observed when the pump is circularly polarized, especially since conventional SBS theory posits that its strength (and hence dynamics) is identical regardless of the polarization state of the pump [23]. Instead, we find that the Stokes light occurs in *only* one mode, which is strictly phase conjugated with respect to the pump. We note that the SBS phase conjugation presented here is produced by stably propagating beams with no mode scrambling, whereas conventional multimode fibers typically experience SBS phase conjugation primarily with aberrated, or speckled, pumps [13,38]. The explanation of this peculiar behavior lies in the fact that a linearly polarized fiber OAM mode is not a single eigenmode, but rather a superposition of two, namely the SOa and SOaa $+\mathcal{L}; \hat{\sigma}^{\pm}$ modes described in section 2. This linear polarization yields optical activity – i.e., a stable rotation of the modes' polarization as it propagates, mimicking a chiral material, as illustrated in Fig. 1(e) and described by Eq. (2). Hence, Eq. (4) is no longer sufficient to characterize this interaction, and we need to additionally invoke the nonlinear photon-phonon amplitude differential equations [23,39], such as $\partial A_{si}/\partial z \propto g_m \tilde{\rho}^* A_{pi}$, which specifically describes an interaction of light in a pump mode, $p = pump$, scattering from an acoustic phonon into a Stokes mode, $s = stokes$. Since the optically active states of the pump and Stokes represent a total of four distinct optical fields, each with two distinct orthogonal polarizations, these differential equations have two components – one where all interacting fields are of the same polarization – the conventional case in single-polarization interactions (already discussed in section 3), and one where they are pair-wise orthogonal, yielding cross-modal SBS interactions. This latter contribution to SBS, relevant for the optically active states, can be represented as:

$$\frac{\partial A_{si}}{\partial z}\bigg|_{cross-modal} \propto \sum_{\mathcal{L}_A = \mathcal{L}_s + \mathcal{L}_p} g_m [A_{pi} A_{pj}^* A_{sj}] \exp(i[\Delta\beta_{ij}(\mathcal{L}_p, \lambda_p) - \Delta\beta_{ij}(\mathcal{L}_s, \lambda_s)]z) \quad (5)$$

where orthogonal polarizations are denoted as i and j (corresponding to $\hat{\sigma}^{\pm}$, respectively), and g_m is the polarization-independent nonlinear gain coefficient proportional to the spatial

overlap strength in Eq. (4). The term $\Delta\beta_{ij}(\mathcal{L}, \lambda) = \beta_i(\mathcal{L}, \lambda) - \beta_j(\mathcal{L}, \lambda)$ is the SOI-induced split in propagation constant between the SOa and SOaa modes of a particular $\mathcal{L}$ and λ. We note that this differential equation maintains the polarization between the pump and Stokes optical fields such that SAM conservation is satisfied. This is because the scalar longitudinal phonons with $\tilde{\rho} \sim A_p \cdot A_s^*$ [1,23] can only be produced by co-polarized pump and Stokes fields, which, in turn can interact *only* with another pair of co-polarized pump and Stokes fields. In addition, as overlap integrals governing g_m mandate, SBS gain is non-negligible only for mode combinations that meet the $\mathcal{L}_A = \mathcal{L}_s + \mathcal{L}_p$ OAM conservation law, which is applied as a constraint in the summation. However, it is also evident that unless $\Delta\beta_{ij}(\mathcal{L}_p, \lambda_p) - \Delta\beta_{ij}(\mathcal{L}_s, \lambda_s) \approx 0$, the cross-modal interaction term will not contribute to any meaningful gain. Ergo, a new phase matching condition has been introduced in which the SOI of both the pump and Stokes modes control the strength of the cross-modal photon-phonon interactions. We demonstrate this principle in Fig. 6(a), where we present calculations of $\Delta\beta_{ij}$ for different $\mathcal{L}$ modes, including for a pump $\mathcal{L}_p = 24$ mode (marked with a black circle) and various $\mathcal{L}_s$ modes frequency shifted 14 GHz away (marked with red, blue, and purple circles). We see that $\Delta\beta_{ij}$ differences are large when $\mathcal{L}_s \neq \mathcal{L}_p$, but almost identical $\Delta\beta_{ij}(\mathcal{L}_p, \nu_p) \approx \Delta\beta_{ij}(\mathcal{L}_s, \nu_s)$ when $\mathcal{L}_s = \mathcal{L}_p$. Since the solution to the differential equations in the undepleted pump regime would be of the form $\text{sinc}^2([\Delta\beta_{ij}(\mathcal{L}_p, \lambda_p) - \Delta\beta_{ij}(\mathcal{L}_s, \lambda_s)]z/2)$, which we will call the phase matching efficiency η, these differences in $\Delta\beta_{ij}$ between $\mathcal{L}_s \neq \mathcal{L}_p$ modes translate to massive reductions in cross-modal gain. We note that in the depleted pump regime where we operate, the effect of the $\eta = \text{sinc}^2([\Delta\beta_{ij}(\mathcal{L}_p, \lambda_p) - \Delta\beta_{ij}(\mathcal{L}_s, \lambda_s)]z/2)$ would still be similar. This is illustrated in Fig. 6(b), where only the phase conjugated $\mathcal{L}_s = \mathcal{L}_p = 24$ SBS process has a non-zero gain efficiency (although even that is slightly reduced on account of its small difference in $\Delta\beta_{ij}$ due to the frequency difference between the pump and Stokes waves). Hence, the only condition that satisfies our new SOI phase matching condition is when $\mathcal{L}_s = \mathcal{L}_p$, and as such, is the only acousto-optic interaction capable of receiving gain from a cross-modal photon-phonon interaction. As a result, with linearly polarized OAM carrying pump modes that experience OA due to SOI, phase conjugation becomes *the* dominant process, allowing it to easily subsume all other processes in the modal competition for growth.

There is a more intuitive explanation for the emergence of the aforementioned phase matching condition for SBS with OAM fiber modes. Recall, from section 2 (see, especially, Fig. 1(e)) that an OA state possesses a unique chiral attribute wherein its amplitude remains constant during fiber propagation but its linear polarization state systematically rotates. The rotation rate is a strong function of topological charge, or OAM content $\mathcal{L}$. Since SBS is highly polarization-selective [1], the SBS interaction that remains non-negligible is the phase conjugated $\mathcal{L}_{stokes} = \mathcal{L}_{pump}$ interaction because this is the only mode that mimics, i.e. retraces, the polarization evolution of the pump (see Fig. 6(c)). However, for all other counter-propagating modes with $\mathcal{L}_{stokes} \neq \mathcal{L}_{pump}$, with Stokes in OAM topological charge of the same (Fig. 6(d)) or opposite (Fig. 6(e)) sign, the rotational behaviors of the pump and Stokes quickly drift apart, resulting in polarization walk-off and low nonlinear gain. Since this rotation rate is intimately tied to the phase difference between the SOa and SOaa modes whose superposition is a linear polarization state, Stokes produced from pumps in OA states depends on an engineered phase matching relationship in an otherwise self-phase matched SBS process. This illustrates a new mechanism of control over SBS with OA: polarization overlap. Since the phase conjugated interaction maximizes the polarization overlap, it is a highly preferred process and receives significant cross-modal photon-phonon gain (see Eq. (5)). Whether one uses the photon-phonon nonlinear amplitude equations or polarization rotational overlap, it is evident that SOI-induced propagation constant splitting in OAM carrying fibers plays a critical role in determining the spatial modes in which substantial SBS gain can be obtained, in sharp contrast to SBS behavior in conventional multimode fibers with standard (i.e. zero-OAM, so-called, LP) modes.
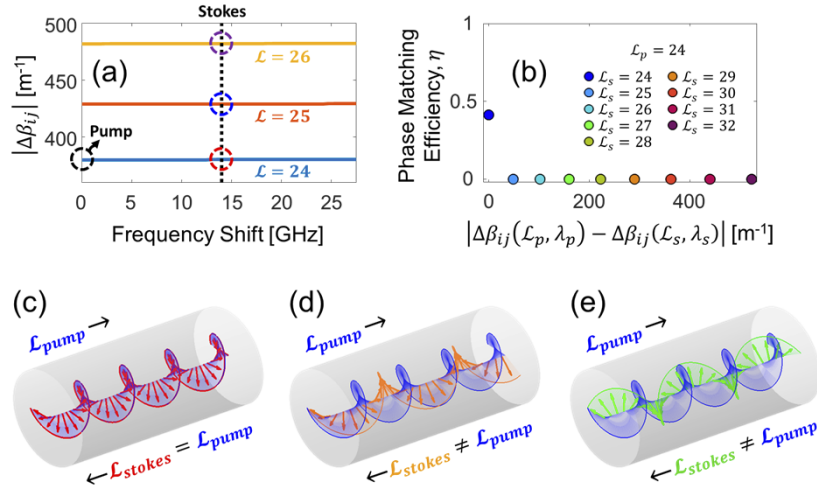
Fig. 6. (a) SOI-induced $\Delta\beta_{ij}$ (between SOa and SOaa modes) calculated over the frequency separation from a $\mathcal{L}_p = 24$ pump at 1045 nm (marked with black circle). Compared to the $\Delta\beta_{ij}$ of the pump, the only $\Delta\beta_{ij}$ that closely matches at the Stokes frequency shift (marked with black line) is when $\mathcal{L}_s = \mathcal{L}_p$ (red circle), whereas all other $\mathcal{L}_s$ modes have large differences in $\Delta\beta_{ij}$ with the pump (blue and purple circles). (b) Phase matching efficiencies η of the cross-modal photon-phonon interaction from Eq. (5) involving a $\mathcal{L}_p = 24$ and various $\mathcal{L}_s$ modes integrated over 50 m of fiber. The only interaction that has a small enough difference in $\Delta\beta_{ij}$ to have a non-negligible efficiency is the phase conjugated process, $\mathcal{L}_s = \mathcal{L}_p$. (c) Evolution of OA rotational states: the forward-propagating $\mathcal{L}_{pump}$ pump OA state is depicted in solid blue. The SBS interaction that receives gain retraces the pump rotation, maximizing polarization overlap, when $\mathcal{L}_{stokes} = \mathcal{L}_{pump}$ (red arrows). On the other hand, when $\mathcal{L}_{stokes} \neq \mathcal{L}_{pump}$, the polarization rotations of the pump and Stokes do not match, meaning the process receives low gain and is essentially suppressed. (d) Depiction of this mismatch between the pump and Stokes modes (orange arrows) with the same chirality, i.e. $+\mathcal{L}_{pump}$ and $+\mathcal{L}_{stokes}$ (e) Depiction of the mismatch between pump and Stokes (green arrows) modes with opposite chirality, i.e. $+\mathcal{L}_{pump}$ and $-\mathcal{L}_{stokes}$.

6. Conclusion

To summarize, the work we present here examines the dynamics of SBS that arise from using a fiber that stably supports a large ensemble of OAM carrying modes. For instance, a simple change in the input polarization state of the pump diverts Stokes-scattered light from occupying several back-propagating modal states to a single phase conjugated state. In contrast, the strength of SBS responses are conventionally considered to be insensitive to the polarization state of the pump. Moreover, while spatial phase conjugation has long been known to occur for SBS, this is primarily in the context of an aberrated pump beam, whereas our experiments used stably propagating modes. This distinctive behavior arises from an inherent chirality induced by linearly polarized light carrying OAM in optical fibers, which introduced a novel, engineerable phase matching criterion, in an otherwise self-phase-matched (SBS) process. OAM conservation laws also imply that the Stokes generated in these fibers are mediated by acoustic modes of record high OAM ($\mathcal{L}_A = 63$) – in fact, the overlap integrals *require* that the spontaneously generated sound waves due to OAM carrying pumps carry roughly twice the topological charge of the optical modes. In general, we show that the angular momentum content of light plays a critical role in controlling the strength, modal content and frequency of the Stokes light, and hence represents an alternative toolbox with which SBS can be controlled in optical fibers.

References

1. A. Kobyakov, M. Sauer, and D. Chowdhury, "Stimulated Brillouin scattering in optical fibers," Adv. Opt. Photonics **2**(1), 1–59 (2010).
2. P. Dragic and J. Ballato, "A Brief Review of Specialty Optical Fibers for Brillouin-Scattering-Based Distributed Sensors," Appl. Sci. **8**(10), 1996 (2018).
3. O. Terra, G. Grosche, and H. Schnatz, "Brillouin amplification in phase coherent transfer of optical frequencies over 480 km fiber," Opt. Express **18**(15), 16102–16111 (2010).
4. Z. Zhu, A. M. C. Dawes, D. J. Gauthier, L. Zhang, and A. E. Willner, "Broadband SBS Slow Light in an Optical Fiber," J. Lightwave Technol. **25**(1), 201–206 (2007).
5. V. I. Kovalev and R. G. Harrison, "Suppression of stimulated Brillouin scattering in high-power single-frequency fiber amplifiers," Opt. Lett. **31**(2), 161–163 (2006).
6. A. Liem, J. Limpert, H. Zellmer, and A. Tünnermann, "100-W single frequency master-oscillator fiber power amplifier," Opt. Lett. **28**(17), 1537–1539 (2003).
7. R. B. Ellis, F. Weiss, and O. M. Anton, "HFC and PON-FTTH networks using higher SBS threshold singlemode optical fibre," Electron. Lett. **43**(7), 405–407 (2007).
8. M. D. Vaughn, A. B. Ruffin, A. Kobyakov, A. Woodfin, C. Mazzali, R. Whitman, A. Boskovic, R. E. Wagner, D. Kozischek, and D. Meis, "Techno-economic study of the value of high stimulated Brillouin scattering threshold single-mode fiber utilization in fiber-to-the-home access networks," J. Opt. Netw. **5**(1), 40–57 (2006).
9. S. V. Tsvetkov, M. M. Khudyakov, A. S. Lobanov, D. S. Lipatov, M. M. Bubnov, A. N. Guryanov, V. Temyanko, and M. E. Likhachev, "SBS Gain Suppression in a Passive Single-Mode Optical Fiber by the Multi-Mode Acoustic Waveguide Design," J. Lightwave Technol. **39**(2), 592–599 (2021).
10. F. W. Willems and W. Muys, "Suppression of interferometric noise in externally modulated lightwave AM-CATV systems by phase modulation," Electron. Lett. **29**(23), 2062–2063 (1993).
11. L. Lombard, A. Brignon, J.-P. Huignard, E. Lallier, and P. Georges, "Beam cleanup in a self-aligned gradient-index Brillouin cavity for high-power multimode fiber amplifiers," Opt. Lett. **31**(2), 158–160 (2006).
12. V. Wang and C. R. Giuliano, "Correction of phase aberrations via stimulated Brillouin scattering," Opt. Lett. **2**(1), 4 (1978).
13. A. Heuer, C. Hänisch, and R. Menzel, "Low-power phase conjugation based on stimulated Brillouin scattering in fiber amplifiers," Opt. Lett. **28**(1), 34–36 (2003).
14. M. Woerdemann, K. Berghoff, and C. Denz, "Dynamic multiple-beam counter-propagating optical traps using optical phase-conjugation," Opt. Express **18**(21), 22348–22357 (2010).
15. S. Sternklar, S. Weiss, and B. Fischer, "Optical Information Processing With The Double Phase Conjugate Mirror," Opt. Eng. **26**(5), 265423 (1987).
16. B. C. Rodgers, T. H. Russell, and W. B. Roh, "Laser beam combining and cleanup by stimulated Brillouin scattering in a multimode optical fiber," Opt. Lett. **24**(16), 1124–1126 (1999).
17. A. Mocofanescu, L. Wang, R. Jain, K. D. Shaw, A. Gavrielides, P. Peterson, and M. P. Sharma, "SBS threshold for single mode and multimode GRIN fibers in an all fiber configuration," Opt. Express **13**(6), 2019–2024 (2005).
18. Y. Xu, M. Ren, Y. Lu, P. Lu, P. Lu, X. Bao, L. Wang, Y. Messaddeq, and S. LaRochelle, "Multi-parameter sensor based on stimulated Brillouin scattering in inverse-parabolic graded-index fiber," Opt. Lett. **41**(6), 1138–1141 (2016).
19. L. Sheng, L. Huang, J. Yan, S. Qiao, A. Zhang, H. Jin, M. Yuan, T. Qu, and Z. Liu, "Distributed multi-parameter sensing based on the Brillouin scattering effect in orbital angular momentum guiding fiber," Opt. Continuum **1**(1), 133–142 (2022).
20. A. Yao and M. J. Padgett, "Orbital angular momentum: origins, behavior and applications," Adv. Opt. Photonics **3**(2), 161–204 (2011).
21. D.L.P. Vitullo, C.C. Leary, P. Gregg, R.A. Smith, D.V. Reddy, S. Ramachandran, and M.G. Raymer, "Observation of Interaction of Spin and Intrinsic Orbital Angular Momentum of Light," Phys. Rev. Lett. **118**, 083601 (2017).
22. A. P. Greenberg, G. Prabhakar, and S. Ramachandran, "High resolution spectral metrology leveraging topologically enhanced optical activity in fibers," Nat Commun **11**(1), 5257 (2020).
23. R.W. Boyd, *Nonlinear Optics*, Elsevier, ed. 4, 2020 (Chap. 9)
24. X. Liu, Z. Ma, A. Antikainen, and S. Ramachandran, "Systematic control of Raman scattering with topologically induced chirality of light," arXiv:2108.03330 (2021)
25. S. D. Johnson, Z. Ma, M. J. Padgett, and S. Ramachandran, "Measurement of the spin-orbit coupling interaction in ring-core optical fibers," OSA Continuum **2**(10), 2975–2982 (2019).

26. P. Vaity, J. Banerji, and R. P. Singh, "Measuring the topological charge of an optical vortex by using a tilted convex lens," Phy. Lett. A **377**(15), 1154–1156 (2013).

27. P. Gregg, P. Kristensen, and S. Ramachandran, "Conservation of orbital angular momentum in air-core optical fibers," Optica **2**(3), 267–270 (2015).

28. X. Zeng, W. He, M. H. Frosz, A. Geilen, P. Roth, G. K. L. Wong, P. S. J. Russell, and B. Stiller, "Stimulated Brillouin scattering in chiral photonic crystal fiber," Photonics Res. **10**(3), 711–718 (2022).

29. H. H. Diamandi, G. Bashan, Y. London, K. Sharma, K. Shemer, and A. Zadok, "Interpolarization Forward Stimulated Brillouin Scattering in Standard Single-Mode Fibers," Laser Photonics Rev. **16**(1), 2100337 (2022).

30. P. Z. Dashti, F. Alhassen, and H. P. Lee, "Observation of Orbital Angular Momentum Transfer between Acoustic and Optical Vortices in Optical Fiber," Phys. Rev. Lett. **96**(4), 043604 (2006).

31. G. Prabhakar, X. Liu, J. Demas, P. Gregg, and S. Ramachandran, "Phase Conjugation in OAM fiber modes via Stimulated Brillouin Scattering," in *Conference on Lasers and Electro-Optics, OSA Technical Digest (online)* (Optical Society of America, 2018), paper FTh1M.4

32. A. Minardo, R. Bernini, and L. Zeni, "Experimental and numerical study on stimulated Brillouin scattering in a graded-index multimode fiber," Opt. Express **22**(14), 17480–17489 (2014).

33. G. L. Keaton, M. J. Leonardo, M. W. Byer, and D. J. Richard, "Stimulated Brillouin scattering of pulses in optical fibers," Opt. Express **22**(11), 13351 (2014).

34. A. Yeniay, J. M. Delavaux, and J. Toulouse, "Spontaneous and Stimulated Brillouin Scattering Gain Spectra in Optical Fibers," J. Lightwave Technol. **20**(8), 1425–1432 (2002).

35. N. Bozinovic, S. Golowich, P. Kristensen, and S. Ramachandran, "Control of orbital angular momentum of light with optical fibers," Opt. Lett. **37**(13), 2451–2453 (2012).

36. S. Preussler and T. Schneider, "Attometer resolution spectral analysis based on polarization pulling assisted Brillouin scattering merged with heterodyne detection," Opt. Exp. **23**(20), 26879–26887 (2015).

37. Z. Ma, P. Kristensen, and S. Ramachandran, "Light guidance beyond cutoff in optical fibers," in *Conference on Lasers and Electro-Optics, OSA Technical Digest* (Optica Publishing Group, 2020), paper SF1P.2

38. S. C. Matthews and D. A. Rockwell, "Correction of phase and depolarization distortions in a multimode fiber at 1.064 μm with stimulated-Brillouin-scattering phase conjugation," Opt. Lett. **19**(21), 1729–1731 (1994).

39. R. Stolen, "Polarization effects in fiber Raman and Brillouin lasers," IEEE J. Quantum Electron. **15**(10), 1157–1160 (1979).